

# Temporal evolution of the nanostructure of Al(Sc,Zr) alloys: Part II-coarsening of $\text{Al}_3(\text{Sc}_{1-x}\text{Zr}_x)$ precipitates

Christian B. Fuller<sup>a,b</sup>, David N. Seidman<sup>a,\*</sup>

<sup>a</sup> Department of Materials Science and Engineering, Northwestern University, 2220 Campus Drive, Evanston, IL 60208-3108, USA

<sup>b</sup> Rockwell Scientific, 1049 Camino Dos Rios, Thousand Oaks, CA 91360, USA

Received 16 April 2005; received in revised form 9 August 2005; accepted 12 August 2005

Available online 10 October 2005

## Abstract

The coarsening behavior of four Al(Sc,Zr) alloys containing small volume fractions (<0.01) of  $\text{Al}_3(\text{Sc}_{1-x}\text{Zr}_x)$  ( $L1_2$ ) precipitates was investigated employing conventional transmission electron microscopy (CTEM) and high-resolution electron microscopy (HREM). The activation energies for diffusion-limited coarsening were obtained employing the Umantsev–Olson–Kuehmann–Voorhees (UOKV) model for multi-component alloys. The addition of Zr is shown to retard significantly the coarsening rate and stabilize precipitate morphologies. HREM of Al(Sc,Zr) alloys aged at 300 °C reveals  $\text{Al}_3(\text{Sc}_{1-x}\text{Zr}_x)$  precipitates with sharp facets parallel to {100} and {110} planes. Coarsening of Al-0.07 Sc-0.019 Zr at.%, Al-0.06 Sc-0.005 Zr at.% and Al-0.09 Sc-0.047 Zr at.% alloys is shown to be controlled by volume diffusion of Zr atoms, while coarsening of Al-0.14 Sc-0.012 Zr at.% is controlled by volume diffusion of Sc atoms.  
© 2005 Acta Materialia Inc. Published by Elsevier Ltd. All rights reserved.

**Keywords:** Al–Sc–Zr; Phase transformations; Nanostructure; Transmission electron microscopy; Coarsening

## 1. Introduction

The temporal evolution of the nanostructure of an aged Al(Sc,Zr) alloy is reported in Part I [1], utilizing high-resolution electron microscopy (HREM) and atom-probe tomography (APT). APT analysis is the only method that yields directly precipitate compositions; the analyses of precipitates shows that Zr substitutes for Sc in  $\text{Al}_3\text{Sc}$  precipitates to form  $\text{Al}_3(\text{Sc}_{1-x}\text{Zr}_x)$  precipitates, where their composition is temporally evolving. Zirconium diffuses four orders of magnitude slower than Sc in Al at 300 °C [2,3], and after aging at 300 °C for 2412 h the  $\text{Al}_3(\text{Sc}_{1-x}\text{Zr}_x)$  precipitates have not achieved global thermodynamic equilibrium; we propose that Al(Sc,Zr) alloys do not reach a global equilibrium, within reasonable time periods, when aged between 300 and 375 °C. In addition, the temporal evolution of  $\text{Al}_3(\text{Sc}_{1-x}\text{Zr}_x)$  precipitates does not achieve a stationary state. This article examines the morphological

and temporal evolution of  $\text{Al}_3(\text{Sc}_{1-x}\text{Zr}_x)$  precipitates employing conventional transmission electron microscopy (CTEM), which is necessary to understand fully the temporal evolution of this system.

The seminal model for diffusion-limited coarsening of binary alloys was developed by Lifshitz and Slyozov [4] and Wagner [5] (LSW model), which assumes: (i) no elastic interactions occur between precipitates, thereby limiting the precipitate volume fraction to zero; (ii) the diffusion fields of precipitates do not overlap; (iii) dilute solid-solution theory obtains; (iv) coarsening occurs in a stress-free matrix; (v) the linearized version of the Gibbs–Thomson equation is valid; (vi) precipitates have a spherical morphology and (vii) precipitates coarsen with a fixed chemical composition. A general analytical approach for determining the diffusion-limited coarsening rate in multi-component alloys was first described by Umantsev and Olson, UO model [6]. Later, the specific case of steady-state coarsening in ternary alloys, which includes capillary effects, was solved by Kuehmann and Voorhees, KV model [7]. Collectively, the Umantsev and Olson [6] and Kuehmann and Voorhees

\* Corresponding author. Tel.: +1 847 491 4391.

E-mail address: [d-seidman@northwestern.edu](mailto:d-seidman@northwestern.edu) (D.N. Seidman).

[7] approaches are denoted the Umantsev–Olson–Kuehmann–Voorhees (UOKV) model. As indicated in Part I [1], there are three temporal equations that describe diffusion-limited coarsening in the asymptotic limit, which are derived for ternary alloys assuming an ideal dilute solution with the off-diagonal terms of the diffusion tensor equal to zero [7]. The first equation describes the increasing average precipitate radius,  $\langle R(t) \rangle$ , as a function of aging time

$$\langle R(t) \rangle^3 - \langle R(0) \rangle^3 = \frac{8\gamma V_m}{9R_g T \left[ \frac{C_{Sc}^\alpha (1 - k_{Sc})^2}{D_{Sc}} + \frac{C_{Zr}^\alpha (1 - k_{Zr})^2}{D_{Zr}} \right]} t, \quad (1)$$

where  $\langle R(t) \rangle$  is the average radius at time  $t$ ,  $\langle R(0) \rangle$  is the average radius at  $t = 0$ , here the superscripts  $\alpha$  and  $\beta$  refer to the  $\alpha$ -Al matrix and  $\text{Al}_3(\text{Sc}_{1-x}\text{Zr}_x)$  precipitate phases, respectively,  $V_m$  is the molar volume of an  $\text{Al}_3(\text{Sc}_{1-x}\text{Zr}_x)$  precipitate,  $\gamma$  is an isotropic interfacial free energy,  $R_g$  is the ideal gas constant,  $T$  is the absolute temperature,  $C_i^\alpha$  is the composition of the  $i$ th component in the matrix,  $D_i$  is the diffusion coefficient of the  $i$ th component in the matrix, and  $k_i$  is the distribution coefficient of the  $i$ th species between the  $\alpha$ -Al and  $\text{Al}_3(\text{Sc}_{1-x}\text{Zr}_x)$  phases and is defined by  $k_i^\beta/C_i^\beta$ . The right-hand side of Eq. (1) is also given by  $k_{KV}t$ , where  $k_{KV}$  is the KV coarsening rate constant. The value used ideally for  $\langle R(0) \rangle$  is for a system in a stationary state. The second equation describes the decreasing precipitate number density,  $N_V(t)$ , with increasing aging time

$$N_V(t) \cong \frac{R_g T V_V \left[ \frac{C_{Sc}^\alpha (1 - k_{Sc})^2}{D_{Sc}} + \frac{C_{Zr}^\alpha (1 - k_{Zr})^2}{D_{Zr}} \right]}{4.21\gamma V_m} t^{-1}, \quad (2)$$

where  $V_V$  is the precipitate volume fraction. The third equation is utilized in Part I [1] for describing the decreasing  $\alpha$ -Al matrix solute composition,  $C_i^\alpha(t)$ , with increasing aging time

$$\begin{aligned} & [C_i^\alpha(t) - C_i^\alpha(t \rightarrow \infty)] \\ &= \frac{2\gamma V_m k_{\text{exp}}^{-1/3} (C_i^\beta - C_i^\alpha)}{R_g T \left[ C_{Sc}^\alpha (1 - k_{Sc})^2 + C_{Zr}^\alpha (1 - k_{Zr})^2 \right]} t^{-1/3}, \end{aligned} \quad (3)$$

where  $C_i^\alpha(t \rightarrow \infty)$  is the equilibrium solid-solubility of the  $i$ th component in the  $\alpha$ -Al matrix, and  $k_{\text{exp}}$  is the experimentally determined coarsening rate constant. The quantity in the brackets on the left-hand side of Eq. (3) is denoted the matrix supersaturation. Eqs. (1)–(3) have the same time dependencies as diffusion-limited coarsening in binary alloys [8–10], but the coarsening rate constants (the coefficients of  $t^n$ ) are significantly different.

Zirconium can substitute for up to 50% of Sc atoms within  $\text{Al}_3\text{Sc}$  precipitates, thus forming  $\text{Al}_3(\text{Sc}_{1-x}\text{Zr}_x)$  (where  $x \leq 0.5$ ) [11,12]. Zirconium additions reduce the lattice parameter of  $\text{Al}_3\text{Sc}$  [13] and concomitantly the interfacial free and elastic strain energies. Furthermore, the diffusivity of Sc in Al is over four orders of magnitude greater than that of Zr in Al at 300 °C [2,3]. Zirconium is, therefore, effective in reducing the coarsening rate of

$\alpha$ -Al– $\text{Al}_3(\text{Sc}_{1-x}\text{Zr}_x)$  alloys, as confirmed earlier by electrical conductivity [14] and hardness measurements [14,15] and suggested by Robson [16].

Microstructural decomposition studies of Al-0.18 Sc-0.05 Zr at.% [17] and Al-0.24 Sc-0.04 Zr at.% [15] reported microhardness values greater than those of Al(Sc) alloys when aged at or above 350 °C. Both studies attribute the increase in microhardness to the presence of a second precipitate phase,  $\text{Al}_3\text{Zr}$  ( $L_{12}$ ), in addition to  $\text{Al}_3\text{Sc}$ . TEM observations of an Al-0.18 Sc-0.05 Zr alloy, aged at 400 °C for 200 h, demonstrate the presence of large semi-coherent  $\text{Al}_3\text{Sc}$  ( $\langle R \rangle = 26.3$  nm) and smaller coherent  $\text{Al}_3\text{Zr}$  ( $\langle R \rangle = 5.5$  nm) precipitates [17], while energy-dispersive X-ray analyses detected large  $\text{Al}_3\text{Sc}$  precipitates and fine  $\text{Al}_3(\text{Sc}_{1-x}\text{Zr}_x)$  precipitates in coexistence in Al-0.24 Sc-0.04 Zr aged at 400 °C for 17 h [15].

The morphological development of  $\text{Ni}_3\text{X}$  ( $L_{12}$ ) precipitates ( $X = \text{Al, Si, Ge, Ti}$  or  $\text{Ga}$ ) in FCC Ni-rich solid solution, have been studied extensively [18–25], and are directly comparable to Al(Sc) alloys since they are structurally analogous. Precipitates in nickel-base alloys occur at higher volume fractions (typically  $>0.10$ ) than  $\text{Al}_3\text{Sc}$  precipitates, but the temporal morphological evolutions are similar [26], as both systems have elastically hard precipitates in a soft matrix and similar elastic moduli anisotropies. As  $\text{Ni}_3\text{Al}$  precipitates coarsen in nickel-base alloys, their morphology evolves from spheroids to cuboids to arrays of cuboids (octets) that eventually split into smaller precipitates [20,25]. This morphological evolution is attributed to the elastic self-energy of isolated precipitates and elastic interactions among precipitates. Morphological evolution is found to depend on lattice parameter mismatch, interfacial free energy, and elastic constants, all of which affect directly coarsening kinetics [25].

Because of the small maximum solid-solubility of Sc in Al, 0.23 at.% at 660 °C [27],  $\text{Al}_3\text{Sc}$  precipitate volume fractions in the Al(Sc) system are inherently small ( $<0.01$ ), and therefore, elastic interactions among precipitates can be neglected; the elastic self-energy of an isolated precipitate is, however, anticipated to play a role in the morphological evolution of  $\text{Al}_3\text{Sc}$  precipitates. Recent TEM studies of Al(Sc) alloys demonstrate a morphological development that is qualitatively similar to those observed for Ni-base alloys [26,28]. At low Sc concentrations ( $\leq 0.12$  at.% Sc),  $\text{Al}_3\text{Sc}$  precipitates ( $\langle R \rangle < 20$  nm) are cauliflower-shaped and evolve to spheroids (Al-0.12 at.% Sc [28]) or lobed cubes (Al-0.07 at.% Sc [26]) after aging for  $>72$  h at 350 °C. Higher concentrations of Sc (Al-0.18 at.% Sc) produce faceted or spheroidal  $\text{Al}_3\text{Sc}$  precipitates, which evolve temporally into cuboids upon aging at 400 °C.

Part I [1] presents results utilizing APT and HREM to examine the chemical compositions of  $\text{Al}_3(\text{Sc}_{1-x}\text{Zr}_x)$  precipitates. Part II presents results utilizing TEM and HREM to investigate the temporal coarsening characteristics of  $\text{Al}_3(\text{Sc}_{1-x}\text{Zr}_x)$  ( $L_{12}$ ) precipitates by examining: (1) the morphology of Zr-containing precipitates; (2) how the morphology changes as a function of Zr concentration;

(3) the mechanism(s) of coarsening. This work is part of a research program to deduce the relationships between the nanostructures of two-phase  $\alpha$ -Al–Al<sub>3</sub>(Sc<sub>1-x</sub>Zr<sub>x</sub>) alloys and their mechanical properties at ambient and elevated temperatures [13,26,29–45], in particular creep.

## 2. Experimental methods

Alloys and TEM samples were produced using the procedures outlined in Part I [1]. In Table 1, the compositions, calculated equilibrium volume fractions, and Sc/Zr ratios, based on at.% and wt.% concentrations, of the Al(Sc,Zr) alloys investigated in Part II are listed. Homogenization was performed at 648 °C for 72 h, within the single-phase region, followed by water quenching to 24 °C. Samples were then aged, within the two-phase region, at 300, 350 or 375 °C, for times between 1.2 and 2412 h to produce Al<sub>3</sub>(Sc<sub>1-x</sub>Zr<sub>x</sub>) (L1<sub>2</sub>) precipitates.

TEM samples were examined in an Hitachi-H8100 (CTEM) and a JEOL 4000 EXII (HREM), the latter at Argonne National Laboratories, operating at 200 kV. Conventional TEM was performed with samples oriented along the  $\langle 100 \rangle$  or  $\langle 110 \rangle$  type directions, utilizing two-beam diffraction conditions. Dark-field images of the precipitates were formed using four  $\{100\}$  superlattice reflections. The thickness of the foil was determined employing a combination of the convergent two-beam electron diffraction (CBED) and thickness-extinction contour fringe methods. To ensure accurate statistics, a minimum of 400 precipitates was used for each coarsening data point. Precipitate dimensions were determined using image-analysis software (NIH Image). For all morphologies, the dimensions of precipitates were calculated by determining the diameter of an area-equivalent circle, which yields an effective diameter [23]. Determination of precipitate number densities employed Kelly's procedure [46] for projected precipitates without overlap or truncation effects. HREM was performed on samples oriented along the  $[100]$  zone axis, and Al<sub>3</sub>(Sc<sub>1-x</sub>Zr<sub>x</sub>) precipitates were imaged with an objective aperture placed around the incident beam and the surrounding four  $\{100\}$  and four  $\{110\}$  superlattice reflections. This technique [26] resolves clearly the precipitates' lattice fringes, but not the matrix's, and allows for definitive imaging of the  $\alpha$ -Al–Al<sub>3</sub>(Sc<sub>1-x</sub>Zr<sub>x</sub>) heterophase interfaces, which are structurally sharp on an atomic scale.

## 3. Results

### 3.1. Morphological evolution of Al<sub>3</sub>Sc<sub>1-x</sub>Zr<sub>x</sub> precipitates

Aging of ternary alloys at 300 °C produces precipitates with  $\langle R \rangle < 4$  nm. Fig. 1 compares the Al<sub>3</sub>(Sc<sub>1-x</sub>Zr<sub>x</sub>) precipitate morphology, as determined by HREM along the  $\langle 100 \rangle$  direction, for the four Al(Sc,Zr) alloys aged at 300 °C for 576 h. The precipitates are faceted parallel to the  $\{100\}$  and  $\{110\}$  planes, as indicated by the white lines. In contrast to the other Al(Sc,Zr) alloys, Al-0.09 Sc-0.047 Zr (Fig. 1(c)) has distinct faceting along the right edge of the precipitate, while atomic height ledges (arrow) are seen along the top left-side of the precipitate. The inset diffraction pattern (Fig. 1(b)) exhibits FCC and L1<sub>2</sub> reflections, and no additional extra reflections due to the Al<sub>3</sub>Zr (DO<sub>23</sub>) phase.

Fig. 2 exhibits CTEM images of the Al-0.07 Sc-0.019 Zr alloy, which demonstrates the morphological development of this alloy for different aging times and temperatures.

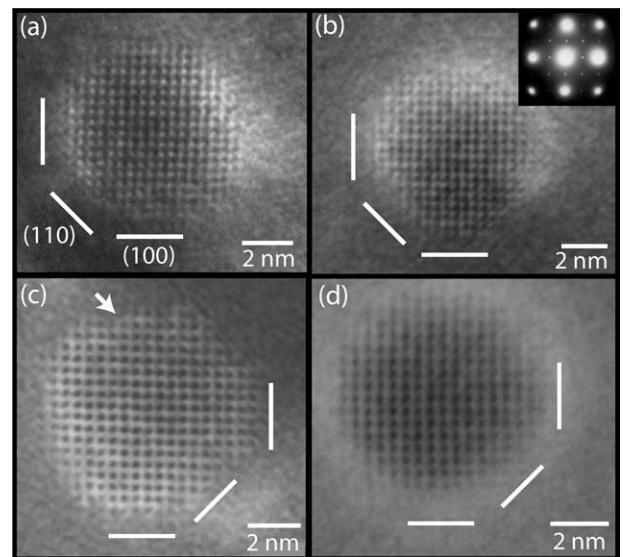


Fig. 1. A comparison of precipitate morphologies as observed employing HREM images,  $[100]$  zone axis, of alloys aged at 300 °C for 576 h: (a) Al-0.06 Sc-0.005 Zr; (b) Al-0.07 Sc-0.019 Zr; (c) Al-0.09 Sc-0.047 Zr; (d) Al-0.14 Sc-0.012 Zr. The arrow in (c) denotes the presence of an atomic height ledge.

Table 1  
Compositions, volume fractions, and Sc/Zr ratios of alloys investigated

Alloy (at.%)	Sc (wt.%)	Zr (wt.%)	Precipitate volume fraction ( $V_V$ ) <sup>a</sup>	Sc/Zr ratio	
				(at.%/at.%)	(wt.%/wt.%)
Al-0.06 Sc-0.005 Zr	0.10	0.018	0.0030	12	5.6
Al-0.07 Sc-0.019 Zr	0.11	0.06	0.0038	3.7	1.8
Al-0.09 Sc-0.047 Zr	0.15	0.16	0.0071	1.9	0.9
Al-0.14 Sc-0.012 Zr	0.24	0.04	0.0074	11.7	6

<sup>a</sup> Calculated from thermodynamic data at 300 °C [1].

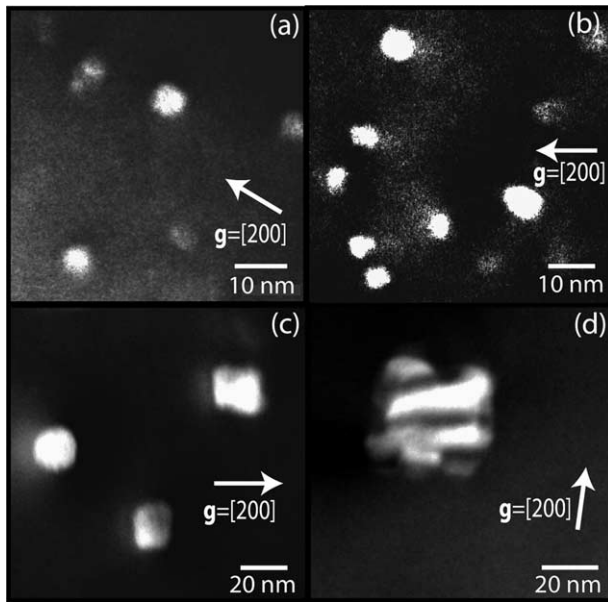


Fig. 2. A comparison of precipitate morphologies as observed employing superlattice dark-field CTEM images (utilizing a 100 superlattice reflection near the [100] zone axis) of Al-0.07 Sc-0.019 Zr aged at: (a) 300 °C for 288 h; (b) 300 °C for 2412 h; (c) 350 °C for 288 h; (d) 375 °C for 196 h.

After aging at 300 °C for 288 h (Fig. 2(a)) or 2412 h (Fig. 2(b)),  $\text{Al}_3(\text{Sc}_{1-x}\text{Zr}_x)$  precipitates exhibit a spheroidal shape, with  $\langle R \rangle < 3$  nm. Increasing the aging temperature to 350 °C, for an aging time of 288 h, produces a combination of spheroidal and cuboidal precipitates (Fig. 2(c)), with  $\langle R \rangle = 8.1 \pm 0.4$  nm. Aging at 375 °C for approximately the same time, 192 h, produces lobed-shaped cuboidal precipitates ( $\langle R \rangle = 23.3 \pm 1.2$  nm, Fig. 2(d)), where the lobes form along  $\langle 111 \rangle$ -type directions.

The effect of solute concentration is displayed in Fig. 3 for Al(Sc,Zr) alloys aged at 375 °C for 192 h. In comparison to the other alloys, Al-0.06 Sc-0.005 Zr has the lowest precipitate volume fraction (0.0029) and the largest precipitate radii ( $\langle R \rangle = 26.9 \pm 1.4$  nm). When this alloy is aged at 375 °C, the morphology is lobed cuboidal precipitates, Fig. 3(a). The dotted arrows indicate misfit interfacial dislocations, which demonstrate a partial loss in coherency for precipitates for this  $\langle R \rangle$  and larger. The larger Zr concentration in Al-0.07 Sc-0.019 Zr produces a larger precipitate volume fraction (0.0036) and a smaller precipitate radius ( $\langle R \rangle = 23.3 \pm 1.2$  nm, Fig. 3(b)). Increasing the precipitate volume fraction (Al-0.09 Sc-0.047 Zr) decreases the precipitate radius ( $\langle R \rangle = 10.6 \pm 0.5$  nm), and produces a combination of spheroidal and cuboidal precipitates (Fig. 3(c)); in contrast, the Al-0.14 Sc-0.012 Zr (volume fraction = 0.0072) alloy contains spheroidal precipitates with  $\langle R \rangle = 5.4 \pm 0.3$  nm (Fig. 3(d)). Spheroidal and cuboidal  $\text{Al}_3(\text{Sc}_{1-x}\text{Zr}_x)$  precipitates are uniformly distributed throughout the matrix, while lobed cuboidal precipitates form in isolation and in lines associated with dislocations, indicating that the latter are heterogeneously nucleated.

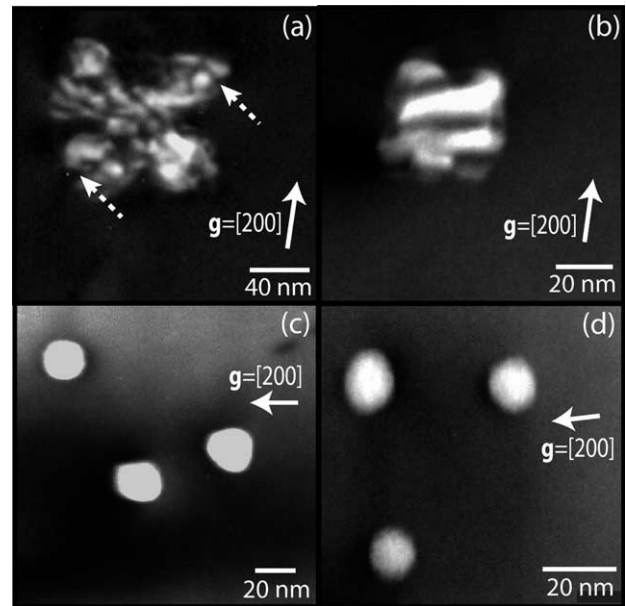


Fig. 3. A comparison of precipitate morphologies as observed employing superlattice dark-field CTEM images (utilizing a 100 superlattice reflection near the [100] zone axis) of alloys aged at 375 °C for 192 h: (a) Al-0.06 Sc-0.005 Zr; (b) Al-0.07 Sc-0.019 Zr; (c) Al-0.09 Sc-0.047 Zr; (d) Al-0.14 Sc-0.012 Zr. The dotted arrows in (a) indicate the presence of interfacial misfit dislocations.

### 3.2. Precipitate size distributions

Precipitate size distributions (PSDs) are produced from histograms of the PSD function ( $g$ ) plotted as a function of normalized radius ( $u = R/\langle R \rangle$ ). PSDs are displayed for the Al-0.14 Sc-0.012 Zr alloy aged at: (1) 300 °C for 288 h (Fig. 4(a)) and 2412 h (Fig. 4(b)); (2) 350 °C for 72 h (Fig. 4(c)) and 2328 h (Fig. 4(d)) and (3) 375 °C for 3 h (Fig. 4(e)) and 192 h (Fig. 4(f)). Precipitates with radii smaller than 2 nm are below the conventional TEM resolution limit, thus the smallest precipitates could be undercounted. Calculated PSDs, according to the LSW and Brailsford–Wynblatt (BW [47]) models, are superimposed on the experimental data. The BW model includes a correction for precipitate volume fraction that decreases the peak height relative to LSW model; recall that the LSW model assumes a precipitate volume fraction approaching zero. The PSDs for aging at 300 and 350 °C have a similar broadness and an increased height relative to those predicted by both models, while the 375 °C PSDs are narrower and taller than predicted by both models. Other coarsening models contain precipitate volume fraction corrections [48], but at small volume fractions ( $< 0.01$ ) all models predict the same result, which is represented in this article by the BW model.

### 3.3. Time exponents for coarsening

Coarsening data is displayed by plotting  $\langle R(t) \rangle$  as a function of time on a double logarithmic plot, Eq. (1). Fig. 5 is

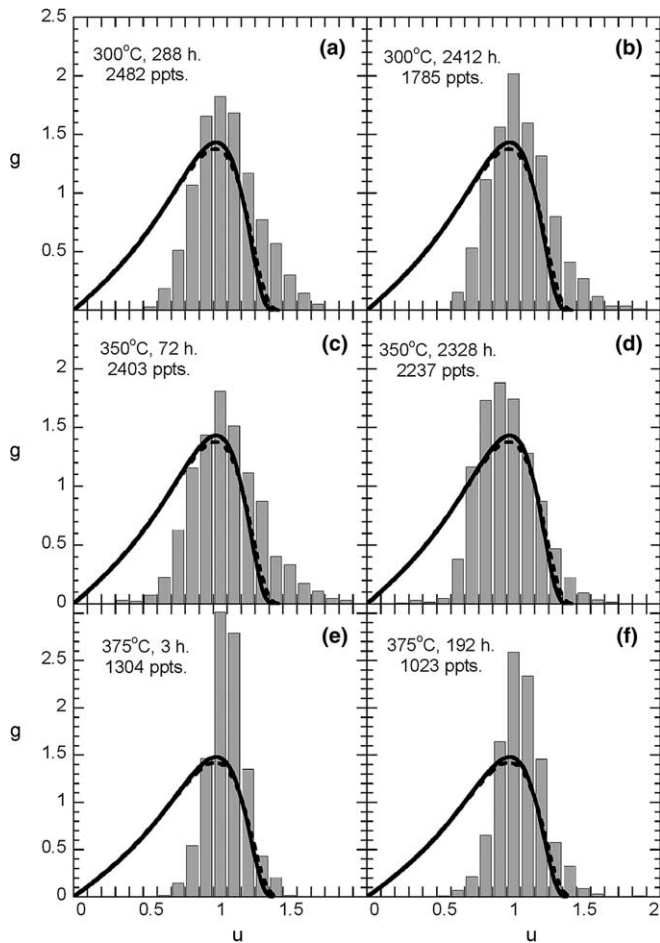


Fig. 4. Examples of precipitate size distributions (PSDs), in which histograms of the PSD function,  $g$ , are plotted as a function of normalized radius,  $u = R/\langle R \rangle$ . These distributions are for an Al-0.14 Sc-0.012 Zr alloy aged at: 300 °C for (a) 288 h and (b) 2412 h; 350 °C for (c) 72 h and (d) 2328 h and 375 °C for (e) 12 h and (f) 192 h. The predictions of the LSW (solid line) [4,5] and BW (dashed line) [47] models are shown for comparison.

a compilation of the coarsening behavior of Al-0.06 Sc-0.005 Zr, Al-0.07 Sc-0.019 Zr, Al-0.09 Sc-0.047 Zr, and Al-0.14 Sc-0.012 Zr alloys at aging temperatures between 300 and 375 °C. The slopes of Fig. 5 yield the time exponents for coarsening, which are equal to 0.1 or less, with the exception of 0.21 (Table 2), and all are significantly smaller than the 1/3 value predicted in Eq. (1). This is in distinct contrast to Al-0.18 at.% Sc, which yields a slope of ca. 1/3 (Fig. 5(a) and (b)). The time exponent for Eq. (2) is determined from a double logarithmic plot of precipitate number density,  $N_V(t)$ , vs. aging time, and values are

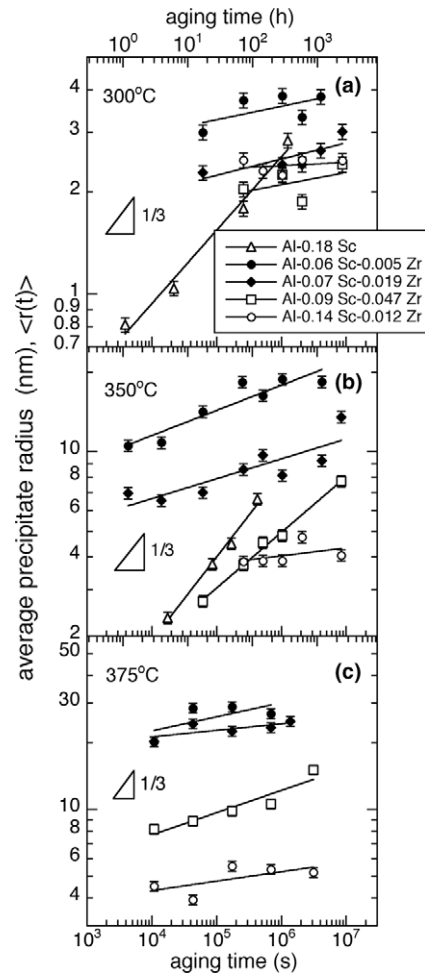


Fig. 5. Double natural logarithmic plot of average precipitate radius,  $\langle R \rangle$ , vs. aging time for indicated alloys at: (a) 300 °C; (b) 350 °C; and (c) 375 °C. The data for the binary Al-0.18 at.% Sc alloy are from [26].

given in Fig. 6 and Table 3. The exponents range from 0.00072 to  $-0.39$ , which are all considerably smaller than the predicted value of  $-1$ . Depletion of the matrix concentration as a function of aging time, as predicted by Eq. (3), is plotted in Fig. 14 of Part I [1]; the resulting time exponents for coarsening at 300 °C are  $-0.33$  for Sc and  $-0.11$  for Zr, compared to the model value of  $-1/3$ . In Part I, we showed that the precipitate composition is temporally evolving. Thus, the three measured time exponents for coarsening indicate that Al(Sc,Zr) alloys do not follow the temporal predictions of the quasi-stationary-state KV model for a ternary alloy.

Table 2

Experimental time exponents for coarsening from the relation of  $\langle R(t) \rangle$  vs.  $t$  (Fig. 5)

	Al-0.06 Sc-0.005 Zr	Al-0.07 Sc-0.019 Zr	Al-0.09 Sc-0.047 Zr	Al-0.14 Sc-0.012 Zr
300 °C	$0.04 \pm 0.01$	$0.03 \pm 0.02$	$0.05 \pm 0.03$	$0.02 \pm 0.01$
350 °C	$0.10 \pm 0.01$	$0.08 \pm 0.01$	$0.21 \pm 0.01$	$0.07 \pm 0.02$
375 °C	$0.06 \pm 0.02$	$0.03 \pm 0.01$	$0.07 \pm 0.01$	$0.02 \pm 0.01$

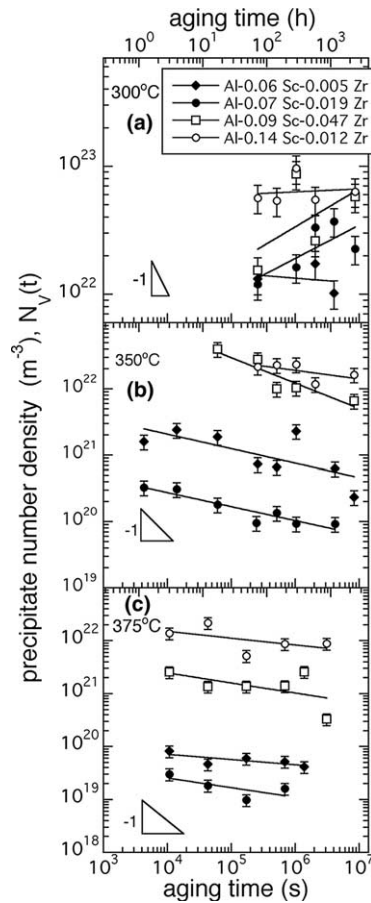


Fig. 6. Double natural logarithmic plot of precipitate number density,  $N_V$ , vs. aging time for indicated alloys at: (a) 300 °C; (b) 350 °C; and (c) 375 °C.

## 4. Discussion

### 4.1. Morphological evolution of $Al_3(Sc_{1-x}Zr_x)$ precipitates

The balance between isotropic interfacial and elastic energies of precipitates dictates the morphology of coherent precipitates [49]. When the precipitate surface-area-to-volume ratio is large, as is the case for small  $Al_3(Sc_{1-x}Zr_x)$  precipitates, the morphology is determined by the minimization of the isotropic interfacial free energy, leading to approximately spheroidal precipitates as observed in Figs. 1, 2(a,b) and 3(d). In contrast, when the  $Al_3(Sc_{1-x}Zr_x)$  precipitate surface-area-to-volume ratio is small, it is the elastic strain energy that determines the morphology. For the case, when the precipitate is elastically stiffer than the matrix, that is,  $C_{44}^{\text{precipitate}} \gg C_{44}^{\text{matrix}}$  ( $C_{44}$  is the shear modulus),

the cuboidal morphology dominates (Figs. 2(c) and 3(c)), while the plate-like morphology dominates when the matrix is elastically stiffer than the precipitate.

The equilibrium shape of precipitates, when dictated by the anisotropy of interfacial free energy, is deduced from Wulff plots [49], utilizing anisotropic interfacial free energy values from the literature, if available. Employing a HREM to investigate Al-0.18 at.% Sc aged at 300 °C, Marquis and Seidman [26] determined that the equilibrium shape for  $Al_3Sc$  precipitates is the great rhombicuboctahedron, which has 6{100}, 12{110}, and 8{111} facets. In Fig. 3,  $Al_3(Sc_{1-x}Zr_x)$  precipitates are observed to have facets parallel to the {100} and {110} planes, which appear to be nearly equal in length to those observed in the Al-0.18 at.% Sc alloy, indicating that the anisotropy of the interfacial free energy for  $Al_3Sc$  and  $Al_3(Sc_{1-x}Zr_x)$  precipitates is similar.

HREM observations [26] demonstrate irregularly shaped precipitates with no facets in Al-0.07 at.% Sc aged at 300 °C for 72 h. The irregular shapes are attributed to growth instabilities caused by the low Sc supersaturation in the matrix; at a constant aging temperature the volume fraction is directly proportional to the supersaturation. Additions of Zr to the Al-0.07 at.% Sc alloy stabilize the morphology of  $Al_3(Sc_{1-x}Zr_x)$  precipitates, such that clear facets parallel to the {100} and {110} planes are observed (Fig. 1(a) and (b)). While the Al-0.06 Sc-0.005 Zr and Al-0.07 Sc-0.019 Zr alloys we investigated have slightly higher volume fractions (0.0031 and 0.0038, respectively) than the binary alloy [26] (0.0026), we believe that the small change in volume fraction does not account for the lack of growth instabilities. If growth instabilities are attributed solely to supersaturation, then increasing the supersaturation, (thereby increasing the volume fraction from 0.0026 to 0.0046, which occurs when comparing the Al-0.07 at.% Sc alloy aged at 300 °C [26] to the Al-0.12 at.% Sc alloy aged at 350 °C [28]), should not produce the irregularly shaped precipitates that are observed by CTEM in both binary alloys. The presence of zirconium, therefore, appears to stabilize  $Al_3(Sc_{1-x}Zr_x)$  precipitates against growth instabilities.

The value of  $N_V$  for Al-0.06 Sc-0.005 Zr aged at 300 °C for 576 h is  $(10 \pm 3) \times 10^{21} \text{ m}^{-3}$ , while the  $N_V$  value for Al-0.07 at.% Sc (aged at 300 °C for 576 h) is  $(5 \pm 2) \times 10^{20} \text{ m}^{-3}$  [26]; therefore, adding 0.005 at.% Zr increases  $N_V$  by more than a factor of 20. This demonstrates that Zr additions are highly effective in increasing  $N_V$ , which may be the result of heterogeneous nucleation of  $Al_3Sc$  and/or  $Al_3(Sc_{1-x}Zr_x)$  precipitates on Sc–Sc, Zr–Zr, and/or

Table 3  
Experimental time exponents for coarsening, from the relation of  $N_V$  vs.  $t$  (Fig. 6)

	Al-0.06 Sc-0.005 Zr	Al-0.07 Sc-0.019 Zr	Al-0.09 Sc-0.047 Zr	Al-0.14 Sc-0.012 Zr
300 °C	$-0.04 \pm 0.03$	$0.28 \pm 0.01$	$0.32 \pm 0.09$	$(7.2 \pm 7.1) \times 10^{-4}$
350 °C	$-0.20 \pm 0.04$	$-0.31 \pm 0.03$	$-0.39 \pm 0.06$	$-0.13 \pm 0.08$
375 °C	$-0.27 \pm 0.05$	$-0.29 \pm 0.02$	$-0.19 \pm 0.05$	$-0.04 \pm 0.03$

Sc–Zr dimers or perhaps larger solute clusters. Also a larger Zr concentration increases the supersaturation and therefore the driving force for homogeneous nucleation, and concomitantly the nucleation current, which implies a higher number density of homogeneously nucleated precipitates.

The lobed cuboids (Fig. 3(a) and (b)) are observed only in the Al-0.06 Sc-0.005 Zr and Al-0.07 Sc-0.019 Zr alloys. Since the volume fraction of precipitates is small ( $<0.004$ ) in these alloys, there are minimal elastic and diffusion field interactions between neighboring  $\text{Al}_3(\text{Sc}_{1-x}\text{Zr}_x)$  precipitates; as a result, the  $\text{Al}_3(\text{Sc}_{1-x}\text{Zr}_x)$  precipitate morphology is due to the elastic self-energy of isolated precipitates. The morphology of isolated individual precipitates is rarely observed experimentally because of the presence of elastic and diffusional interactions between precipitates; isolated precipitate morphologies can, however, be calculated, for example, utilizing the discrete atom method [50]. This method treats isolated two-dimensional precipitates in a cubic matrix and finds them to have fourfold symmetry (elongated along the  $[1\ 1]$  and  $[1\ \bar{1}]$  directions), which is not due to the anisotropy of interfacial free energy. This fourfold symmetry is attributed solely to elastic self-energy due to the lattice parameter mismatch and the different elastic anisotropies of the two phases. Similar  $\text{Al}_3(\text{Sc}_{1-x}\text{Zr}_x)$  precipitate morphologies are observed in a binary Al-0.07 at.% Sc alloy containing about the same volume fraction of  $\text{Al}_3\text{Sc}$  precipitates [26].

#### 4.2. Precipitate size distributions (PSDs)

PSDs provide a measure of how well coarsening experiments obey extant coarsening models. PSDs were determined for the Al-0.14 Sc-0.012 Zr alloy, which provides a demonstration of the changes in PSDs as a function of both aging temperature and time. The LSW model for a binary alloy predicts that the PSD shape is time-invariant, that is, it is self-similar, while current coarsening models [51–54] predict a broadening of the PSD and an increase in the rate constant, with a concomitant increase in volume fraction of precipitates. Fig. 4 demonstrates that the full-width at half-maximum of the average experimental PSD does not change significantly when Al-0.14 Sc-0.012 Zr is aged at 300 or 350 °C.

#### 4.3. Coarsening in ternary alloys

##### 4.3.1. Time exponents for coarsening

There have been several investigations of the kinetics of coarsening systems utilizing Eq. (1), which yield time exponents for coarsening ( $\langle R(t) \rangle$  vs.  $t$ ) with values other than  $1/3$  [55–57]. A cluster–diffusion–coagulation model that applies to low temperatures has been developed [55,56], where clusters represent order-parameter fluctuations, and where diffusion of atoms between precipitates is slow. This model proposes that coarsening may occur through the diffusion and coagulation of entire clusters due to solute-atom transport along interfaces, which is governed by how the local

diffusional mechanism affects a shift in a precipitate's center-of-mass. Since the time exponent for coarsening is shown to depend on the spinodal critical temperature ( $T_c$ ), this model [55,56] yields exponents of  $1/6$  (at low temperatures, where  $T$  is much less than  $T_c$ ), and  $1/5$  or  $1/4$  (at intermediate temperatures, where  $T$  is at or slightly above  $T_c$ ). Recent lattice kinetic Monte Carlo simulations [57] demonstrate that coarsening kinetics are a function of the possible different vacancy concentrations in the matrix and precipitate phases. For these simulations, time exponents of coarsening were found to vary from 0.11 to 0.267, depending on where vacancies prefer to diffuse (in matrix or precipitate phases) and the number of time steps in the lattice kinetic Monte Carlo simulation. When vacancies prefer to diffuse inside precipitates, precipitate diffusion and coagulation is favored; conversely, when vacancies prefer to diffuse in the matrix, the classical evaporation–condensation mechanism is favored.

Time exponents for coarsening are derived from the data plotted in Fig. 5. For this procedure to be reliable  $\langle R(0) \rangle \ll k_{\text{LSW}}t$  must be satisfied, which occurs physically when the increase in precipitate radius is large relative to  $\langle R(0) \rangle$ . Therefore, accurate time exponents for coarsening are difficult to calculate, for the Al(Sc,Zr) system, at 300 °C, where precipitates do not significantly coarsen. Thus, the time exponents determined are most likely effective values.

##### 4.3.2. Coarsening mechanisms

Precipitate coarsening may occur by diffusion-limited coarsening, interface-limited coarsening, or a combination of these two mechanisms [58], with interface-limited coarsening occurring at small  $\langle R(t) \rangle$  and diffusion-limited coarsening occurring at larger  $\langle R(t) \rangle$  values. At constant precipitate volume fraction, as is the case for the aging times in this article (Table 4), diffusion-limited coarsening is the most probable mechanism. Analyses of the coarsening results indicate that diffusion-limited coarsening is occurring, which is supported by the agreement of the activation energy values calculated in Section 4.3.2.2 with the literature values.

**4.3.2.1. Experimental coarsening kinetics.** The coarsening kinetics for each ternary alloy at 300, 350, or 375 °C is displayed in Figs. 7 and 8. As anticipated, the coarsening rate for each alloy increases with increasing temperature. Fig. 7 demonstrates that increasing the Zr concentration [Al-0.06 Sc-0.005 Zr (Fig. 7(a)) vs. Al-0.07 Sc-0.019 Zr (Fig. 7(b))] decreases the coarsening rate (slope of the linear fit). To calculate coarsening rates according to Eq. (1),  $\langle R(t) \rangle^3$  is plotted as a function of aging time (Fig. 9), where the slope of the linear regression line is the experimental coarsening rate,  $k_{\text{exp}}$  (Table 4).

The interfacial free energy of coherent precipitates is smaller than that of semi-coherent precipitates, due to the absence of interfacial misfit dislocations. A change in interfacial free energy has a profound impact on the coarsening

Table 4

Experimentally and theoretically determined coarsening rate constants ( $k_{\text{exp}}$  and  $k_{\text{KV}}$ , respectively) and volume fractions ( $V_V$ ) of  $\text{Al}_3(\text{Sc}_{1-x}\text{Zr}_x)$  precipitates for each alloy studied

Alloy (at.%)		300 °C	350 °C	375 °C
Al-0.06 Sc-0.005 Zr	$k_{\text{exp}}$ ( $\text{m}^3 \text{s}^{-1}$ )	$(5.13 \pm 2.07) \times 10^{-33}$	$(1.50 \pm 0.22) \times 10^{-30}$	$(8.27 \pm 4.15) \times 10^{-30}$ $(3.15 \pm 0.54) \times 10^{-29\text{c}}$
	$k_{\text{KV}}$ ( $\text{m}^3 \text{s}^{-1}$ )	$2.2 \times 10^{-35}$	$2.9 \times 10^{-33}$	$2.4 \times 10^{-32}$
	$k_{\text{exp}}/k_{\text{KV}}$	229	522	344
	Exp. $V_V^{\text{a}}$	$(2.7 \pm 0.8) \times 10^{-3}$	$(2.9 \pm 0.7) \times 10^{-3}$	$(2.9 \pm 0.9) \times 10^{-3}$
	Calc. $V_V^{\text{b}}$	$3.1 \times 10^{-3}$	$3.0 \times 10^{-3}$	$2.9 \times 10^{-3}$
Al-0.07 Sc-0.019 Zr	$k_{\text{exp}}$ ( $\text{m}^3 \text{s}^{-1}$ )	$(1.86 \pm 0.55) \times 10^{-33}$	$(1.62 \pm 0.24) \times 10^{-31}$	$(4.12 \pm 1.72) \times 10^{-30}$ $(4.05 \pm 0.75) \times 10^{-29\text{c}}$
	$k_{\text{KV}}$ ( $\text{m}^3 \text{s}^{-1}$ )	$7.2 \times 10^{-36}$	$9.7 \times 10^{-34}$	$8.5 \times 10^{-33}$
	$k_{\text{exp}}/k_{\text{KV}}$	259	166	484
	Exp. $V_V^{\text{a}}$	$(3.3 \pm 0.8) \times 10^{-3}$	$(3.6 \pm 0.7) \times 10^{-3}$	$(3.3 \pm 0.8) \times 10^{-3}$
	Calc. $V_V^{\text{b}}$	$3.8 \times 10^{-3}$	$3.7 \times 10^{-3}$	$3.6 \times 10^{-3}$
Al-0.09 Sc-0.047 Zr	$k_{\text{exp}}$ ( $\text{m}^3 \text{s}^{-1}$ )	$(4.29 \pm 2.58) \times 10^{-34}$	$(6.75 \pm 0.73) \times 10^{-32}$	$(9.1 \pm 1.5) \times 10^{-31}$
	$k_{\text{KV}}$ ( $\text{m}^3 \text{s}^{-1}$ )	$4.7 \times 10^{-36}$	$6.2 \times 10^{-34}$	$5.4 \times 10^{-33}$
	$k_{\text{exp}}/k_{\text{KV}}$	91	109	170
	Exp. $V_V^{\text{a}}$	$(6.8 \pm 2.4) \times 10^{-3}$	$(6.8 \pm 2.0) \times 10^{-3}$	$(6.8 \pm 2.0) \times 10^{-3}$
	Calc. $V_V^{\text{b}}$	$7.1 \times 10^{-3}$	$6.9 \times 10^{-3}$	$6.8 \times 10^{-3}$
Al-0.14 Sc-0.012 Zr	$k_{\text{exp}}$ ( $\text{m}^3 \text{s}^{-1}$ )	$(3.92 \pm 3.37) \times 10^{-34}$	$(9.2 \pm 9.1) \times 10^{-34}$	$(2.61 \pm 0.79) \times 10^{-32}$
	$k_{\text{KV}}$ ( $\text{m}^3 \text{s}^{-1}$ )	$2.2 \times 10^{-35}$	$2.9 \times 10^{-33}$	$2.4 \times 10^{-32}$
	$k_{\text{exp}}/k_{\text{KV}}$	18	0.32	1.1
	Exp. $V_V^{\text{a}}$	$(6.9 \pm 2.1) \times 10^{-3}$	$(6.6 \pm 2.0) \times 10^{-3}$	$(6.7 \pm 2.0) \times 10^{-3}$
	Calc. $V_V^{\text{b}}$	$7.4 \times 10^{-3}$	$7.3 \times 10^{-3}$	$7.2 \times 10^{-3}$

<sup>a</sup> Calculated from:  $V_V = (4/3)\langle r \rangle A'/H$  [46]; where  $A'$  is precipitate areal fraction and  $H$  is the TEM foil thickness, which assumes that precipitates are present in an ideal thin foil.

<sup>b</sup> Calculated from thermodynamic data [1].

<sup>c</sup> Coarsening rate constants after precipitates have lost full coherency.

kinetics of an alloy, as indicated in Eq. (1). A definitive change in the coarsening rate is observed for the Al-0.06 Sc-0.005 Zr and Al-0.07 Sc-0.019 Zr alloys (Fig. 7(a) and (b), respectively) when aged at 375 °C for times longer than 384 h; note the change in slope from  $(8.27 \pm 4.15) \times 10^{-30}$  to  $(3.15 \pm 0.54) \times 10^{-29} \text{ m}^3 \text{ s}^{-1}$  for the Al-0.06 Sc-0.005 Zr alloy and  $(4.12 \pm 1.72) \times 10^{-30}$  to  $(4.05 \pm 0.75) \times 10^{-29} \text{ m}^3 \text{ s}^{-1}$  for the Al-0.07 Sc-0.019 Zr alloy (Table 4). The increase in coarsening rate is most likely due to a change in the interfacial free energy of the precipitates resulting from a partial loss in coherency, which is consistent with observations in Ni-base [19,22], Fe–Cu [49], and Cu–Co [18] alloys. Examples of precipitates and their associated misfit dislocations are displayed in Fig. 10, where Fig. 10(b) shows only the locations of the  $\text{Al}_3(\text{Sc}_{1-x}\text{Zr}_x)$  precipitates and Fig. 10(c) shows the positions of the misfit dislocation cores in relation to the  $\text{Al}_3(\text{Sc}_{1-x}\text{Zr}_x)$  precipitates. We, therefore, calculated coarsening rates and activation energies only for precipitates with  $\langle R \rangle < 30 \text{ nm}$ , where full coherency is assured.

For comparative purposes, Fig. 11 shows the coarsening behavior of the ternary alloys for each aging temperature, along with the binary Al-0.15 at.% Sc alloy aged at 300 and 350 °C [26]. Fig. 11(c) shows the effect of coherency on coarsening rates for the Al-0.06 Sc-0.005 Zr and Al-0.07 Sc-0.019 Zr alloys at 375 °C, where an abrupt change in slope denotes the loss of precipitate coherency, as determined by the presence of misfit dislocations. Thus, partially

coherent precipitates coarsen at a faster rate than fully coherent precipitates. A comparison between the binary Al-0.15 at.% Sc and the volume fraction equivalent Al-0.14 Sc-0.012 Zr alloy demonstrates that Zr additions are effective in decreasing the coarsening rate.

The effect of volume fraction on the coarsening kinetics of Al(Sc,Zr) alloys is examined for the Al-0.06 Sc-0.005 Zr and Al-0.14 Sc-0.012 Zr alloys, which have Sc/Zr (at.%/at.%) ratios near one another (therefore sitting on the same tie-line, Fig. 2 in Part I [1]) and a 58% difference in volume fraction (Table 4). As the precipitate volume fraction is increased from 0.0031 to 0.0074 (Al-0.06 Sc-0.005 Zr and Al-0.14 Sc-0.012 Zr alloys, respectively), the coarsening rate decreases. An inverse relationship between the coarsening rate and precipitate volume fraction has been observed in alloys containing small precipitate volume fractions ( $< 0.04$ ) [10,59,60]. The coarsening rate decreases because of an increase in diffusional and elastic interactions among precipitates, with increasing precipitate volume fraction. In the Al(Sc,Zr) system, the precipitate volume fraction is small enough that diffusional interactions between precipitates may be negligible, but we now examine this point in more detail. The distance for diffusional interaction of precipitates is known as the screening distance, and is calculated to be  $\approx 32\langle R \rangle$  for the Al(Sc,Zr) alloys [61]. When the Al-0.14 Sc-0.012 Zr alloy contains precipitates with  $\langle R \rangle = 3.6 \text{ nm}$ , the screening distance is 115 nm, which is 48% larger than

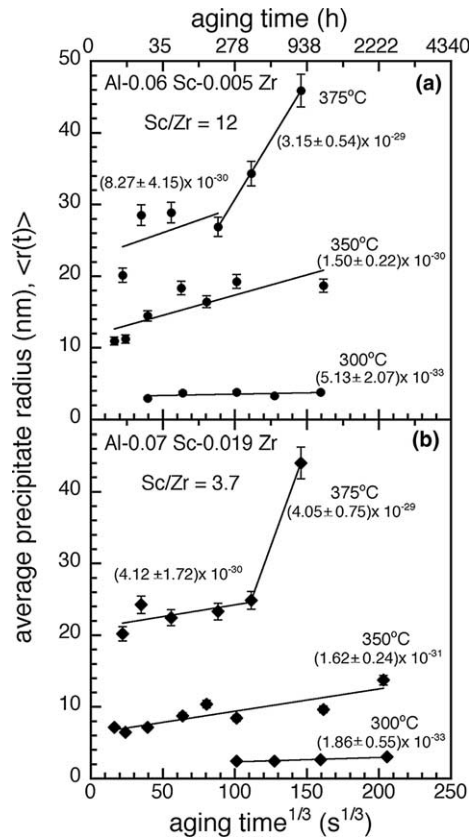


Fig. 7. Coarsening data plotted as average precipitate radius,  $\langle R \rangle$ , vs.  $(\text{time})^{1/3}$  for: (a) Al-0.06 Sc-0.005 Zr and (b) Al-0.07 Sc-0.019 Zr alloys aged at indicated temperatures. Numbers next to each curve are the coarsening rate constants ( $\text{m}^3 \text{s}^{-1}$ ). The sharp change in slope at 375 °C is due to the  $\text{Al}_3(\text{Sc}_{1-x}\text{Zr}_x)$  precipitates losing their full coherency.

the calculated center-to-center interprecipitate distance of 56 nm [42]. Precipitates will, therefore, interact with each other via diffusion. The same calculation for the Al-0.06 Sc-0.005 Zr alloy,  $\langle R \rangle = 3.3$  nm, produces a screening distance of 106 nm, which is 72% larger than the interprecipitate distance of 76 nm. Comparing these percentages (48% for Al-0.14 Sc-0.012 Zr vs. 72% for Al-0.06 Sc-0.005 Zr), an increase in volume fraction corresponds to an increase in diffusional interactions between precipitates.

Ardell has independently determined the interfacial free energy and diffusivity of solute atoms, utilizing the asymptotic solutions of Eqs. (1) and (2) for a binary alloy [9]. Extending Ardell's approach [9] to a ternary alloy [30], the data for the Al-0.09 Sc-0.047 Zr alloy in Part I (the variation in matrix Sc composition, the coarsening rate constant of  $8.47 \pm 4.40 \times 10^{-7} \text{ m}^3 \text{ s}^{-1}$ , and the distribution coefficient for Sc and Zr [1]) is combined with the corresponding coarsening rate constant at 300 °C ( $k_{\text{exp}}$ , Table 4) to determine an interfacial free energy of  $59 \text{ mJ m}^{-2}$ , Eq. (3). This value is smaller than the calculated interfacial free energies for the  $\alpha$ -Al– $\text{Al}_3\text{Sc}$  interface of  $160 \text{ mJ m}^{-2}$  for {100} and  $185 \text{ mJ m}^{-2}$  for {111} orientations at 300 °C [62]. This method assumes the application of the asymptotic solutions to the LSW model, while coarsening of the

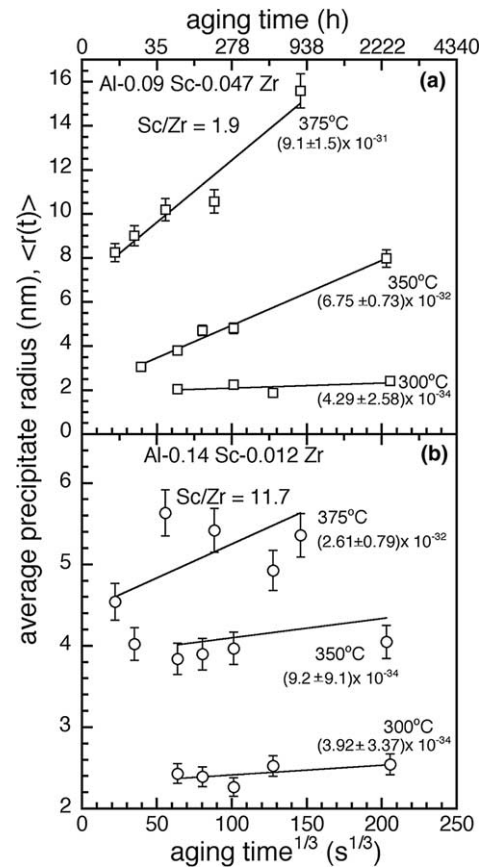


Fig. 8. Coarsening data plotted as average precipitate radius,  $\langle R \rangle$ , vs.  $t^{1/3}$  for: (a) Al-0.09 Sc-0.047 Zr and (b) Al-0.14 Sc-0.012 Zr alloys aged at indicated temperatures. Numbers next to each curve are the coarsening rate constants ( $\text{m}^3 \text{ s}^{-1}$ ).

Al-0.09 Sc-0.047 Zr alloy at 300 °C is shown to be in a non-stationary-state regime [1].

**4.3.2.2. Activation energies for coarsening.** Temperature dependent factors in Eq. (1) are present in the form of the equilibrium solute concentration in the  $\alpha$ -Al matrix and  $\text{Al}_3(\text{Sc}_{1-x}\text{Zr}_x)$  precipitate phases. Since Zr substitutes for Sc within the precipitate phase, the ternary Al–Sc–Zr system can be considered a pseudobinary system ( $\text{Al}_3\text{Sc}$ –Zr system), where the coarsening rate is determined by the element with the smaller volume diffusivity. This approach was utilized to determine the activation energies for diffusion-limited coarsening in studies of ternary Ni–Al–Cr [63] and Al–V–Zr [64] alloys. The activation energies for diffusion-limited coarsening, including temperature dependence, were calculated from the slope of an Arrhenius plot of  $k_{\text{exp}} 9RT(c^\beta - c^\alpha)^2 / 8c^\alpha(1 - c^\alpha)\gamma V_m$  vs. inverse aging temperature (Fig. 12(a)), where Zr is assumed to be the rate-limiting solute element. The resulting temperature corrected activation energies are listed in Table 5 under  $Q_R$ .

A comparison between the temperature corrected activation energies,  $Q_R$  (Table 5), and the activation energies for Sc and Zr diffusion in Al found in the literature (Table 6) demonstrates that Al-0.06 Sc-0.005 Zr, Al-0.07 Sc-0.019

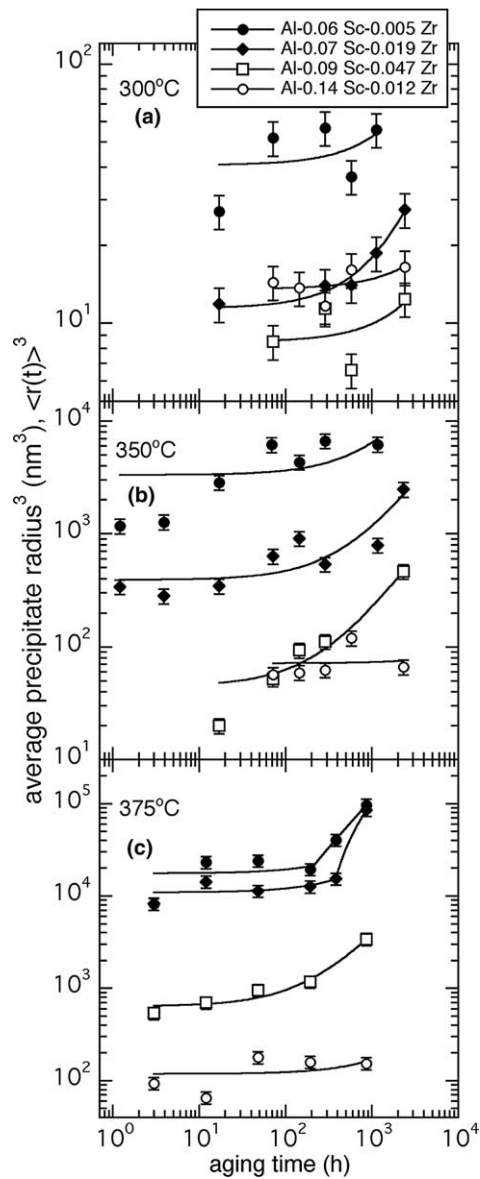


Fig. 9. Double logarithmic plots of  $\langle r \rangle^3$  vs. aging time for indicated alloys at: (a) 300 °C; (b) 350 °C; and (c) 375 °C.

Zr, and Al-0.09 Sc-0.047 Zr have activation energies ( $258 \pm 37$ ,  $240 \pm 15$ , and  $281 \pm 17$  kJ mol<sup>-1</sup>, respectively) near the literature values for Zr in Al ( $222$  [65] and  $242$  kJ mol<sup>-1</sup> [3]). In contrast, Al-0.14 Sc-0.012 Zr has an activation energy ( $Q_R = 134 \pm 28$  kJ mol<sup>-1</sup>), which is near the literature values for Sc in Al ( $174$  [66],  $154$  [67], and  $164 \pm 9$  kJ mol<sup>-1</sup> [26]). Coarsening of precipitates in Al-0.06 Sc-0.005 Zr, Al-0.07 Sc-0.019 Zr, and Al-0.09 Sc-0.047 Zr alloys is therefore controlled by volume diffusion of Zr and coarsening of precipitates in Al-0.14 Sc-0.012 Zr is controlled by volume diffusion of Sc.

**4.3.2.3. Comparison to a ternary coarsening theory.** An illustration of the effects of Zr additions on the normalized KV coarsening rate constant [7],  $\tilde{k}_{KV}$ , is presented in Fig. 13, where  $\tilde{k}_{KV}$  is given by

$$\tilde{k}_{KV} = \frac{k_{KV}}{8\gamma V_m D_{Sc}} \quad (4)$$

Fig. 13 is for  $T = 300$  °C, where the distribution coefficients for the Al-0.06 Sc-0.005 Zr alloy are taken from the tie-line data displayed in Fig. 2 of Part I [1]; it does not, however, require a knowledge of  $\gamma$  and  $V_m$ . Fig. 13 demonstrates quantitatively that the addition of Zr at constant Sc concentration decreases the coarsening rate of Al<sub>3</sub>Sc precipitates.

The tie-line data displayed in Fig. 2 of Part I [1] and the best estimates from the literature for the interfacial energy

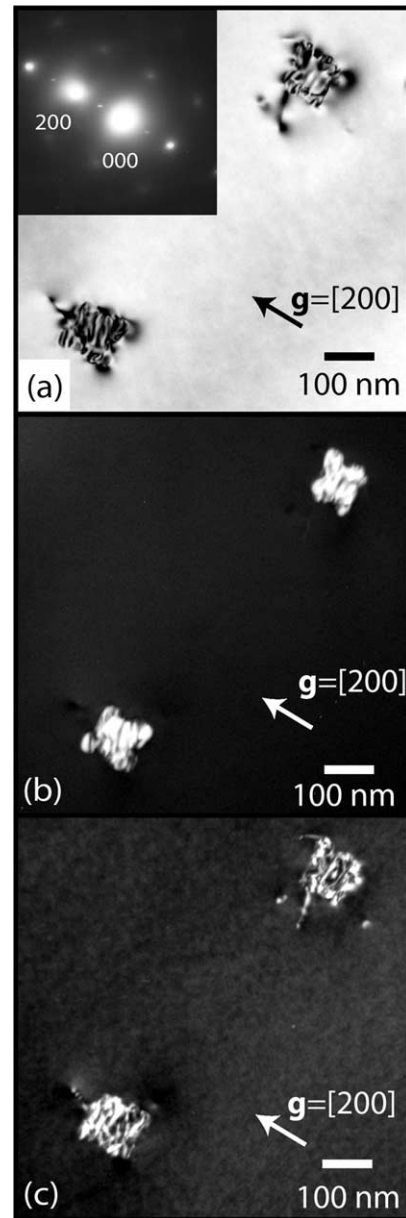


Fig. 10. The presence of interfacial misfit dislocations as observed from: (a) 2-beam bright-field with  $g = [200]$ ; (b) superlattice dark-field with  $g = [200]$  and (c) weak-beam dark-field CTEM images where  $g = [200]$  is the imaging reflection and  $3g$  is the excited reflection. The micrographs are for an Al-0.06 Sc-0.005 Zr alloy aged at 375 °C for 863.5 h.

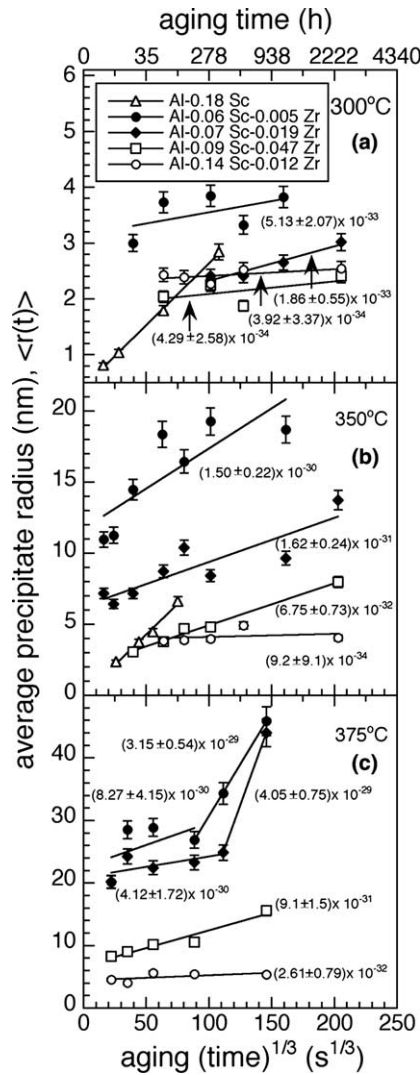


Fig. 11. Coarsening data as given by average precipitate radius,  $\langle R \rangle$ , vs.  $t^{1/3}$  for indicated alloys at: (a) 300 °C; (b) 350 °C; and (c) 375 °C. Numbers next to each curve are the coarsening rate constants ( $\text{m}^3 \text{s}^{-1}$ ). The data for the binary Al-0.18 at.% Sc alloy is from [26].

(175  $\text{mJ m}^{-2}$ ) [62] and the molar volume of the  $\text{Al}_3(\text{Sc}_{1-x}\text{Zr}_x)$  precipitate ( $1.038 \times 10^{-5} \text{ m}^3 \text{ mol}^{-1}$ ), calculated from  $V_m = N_A a^3/4$  ( $N_A$  is Avogadro's number and  $a = 0.410 \text{ nm}$  is the lattice parameter of  $\text{Al}_3\text{Sc}_{0.9}\text{Zr}_{0.1}$  [13]), were utilized to calculate the theoretical coarsening rates,  $k_{KV}$ , for all the Al(Sc,Zr) alloys and aging temperatures. The results are displayed in Fig. 12(b) and Table 4, which are compared to the experimental data ( $k_{exp}$ ) in Fig. 12(a) and Table 4. The ratios of  $k_{exp}/k_{KV}$  (Table 4) indicate that the  $k_{exp}$  values are significantly greater than  $k_{KV}$  values for all alloys aged at 300, 350 or 375 °C, with the exception of Al-0.14 Sc-0.012 Zr at 350 or 375 °C. These calculations were then utilized to determine an effective theoretical activation energy for each alloy ( $Q_{model}$ , Table 5) from the slope of an Arrhenius plot of  $k_{KV} 9RT(c^\beta - c^\alpha)^2/8c^\alpha(1 - c^\alpha)\gamma V_m$  vs. inverse aging temperature (Fig. 12(b)).

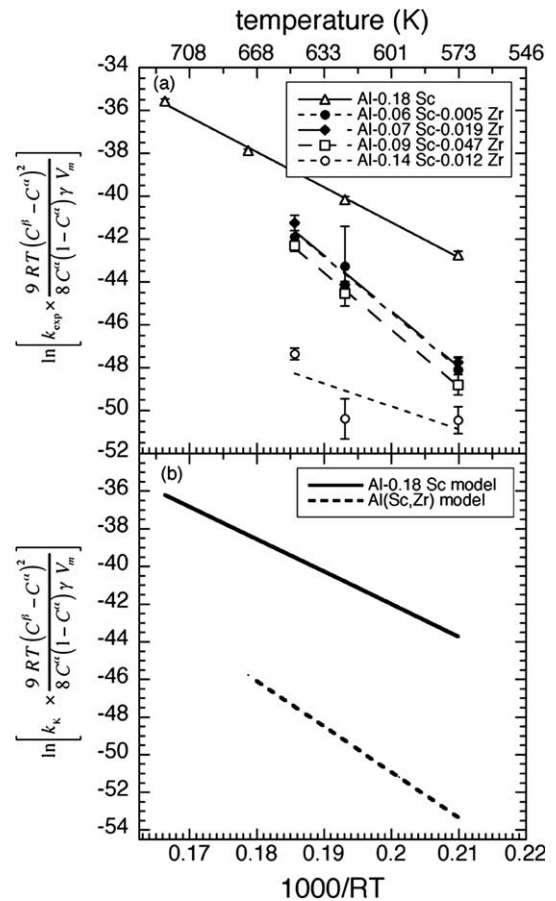


Fig. 12. Arrhenius plots of coarsening rate constant ( $k$ ) vs. inverse aging temperature for: (a) experimental data,  $k = k_{exp}$  and (b) KV model,  $k = k_{KV}$ . Each slope yields the effective activation energy for diffusion-limited coarsening. Data for the Al-0.18 at.% Sc alloy are from [26] (b) displays the theoretical predictions for the alloys shown in (a).

Table 5

Comparison of experimentally determined activation energies

Alloy	$Q_R$ ( $\text{kJ mol}^{-1}$ ) <sup>a</sup>	$Q_{model}$ ( $\text{kJ mol}^{-1}$ ) <sup>b</sup>
Al-0.06 Sc-0.005 Zr	$258 \pm 37$	242
Al-0.07 Sc-0.011 Zr	$240 \pm 15$	242
Al-0.09 Sc-0.047 Zr	$281 \pm 17$	242
Al-0.14 Sc-0.012 Zr	$134 \pm 28$	242

<sup>a</sup> Values were calculated from the slope of the Arrhenius plot of  $k_{exp} 9RT(c^\beta - c^\alpha)^2/8c^\alpha(1 - c^\alpha)\gamma V_m$  vs.  $1/RT$ , where Zr was assumed to be the rate limiting solute element, Fig. 12(a).

<sup>b</sup> Values were calculated from the slope of the Arrhenius plot of  $k_{KV} 9RT(c^\beta - c^\alpha)^2/8c^\alpha(1 - c^\alpha)\gamma V_m$  vs.  $1/RT$ , where Zr was assumed to be the rate limiting solute element, Eq. (1).

The temperature compensated values of  $k_{KV}$  fall onto a single line for the four Al(Sc,Zr) alloys, which, of course, produces equal values of  $Q_{model}$  ( $242 \text{ kJ mol}^{-1}$ , Table 5). It was anticipated that the values of  $Q_{model}$  are equal, since it is assumed that Zr is the rate-limiting diffusing element and the activation energy calculated by tracer diffusion of Zr in Al is  $242 \text{ kJ mol}^{-1}$  [3] (Table 6). The collapsing of the results for four alloys onto a single line demonstrates

Table 6  
Literature values for the diffusivity of Sc or Zr in Al

Solute elements	Method	$D_0$ ( $\text{m}^2 \text{s}^{-1}$ )	$Q$ ( $\text{kJ mol}^{-1}$ )	References
Sc in Al	Tracer diffusivity	$5.31 \times 10^{-4}$	174	[66]
	First-principle calculations	–	154	[67]
	Coarsening measurements	$(1.9 \pm 0.5) \times 10^{-4}$	$164 \pm 9$	[26]
Zr in Al	Tracer diffusivity	$7.28 \times 10^{-2}$	242	[3]
	Coarsening measurements	$5.4 \times 10^{-3}$	222	[65]

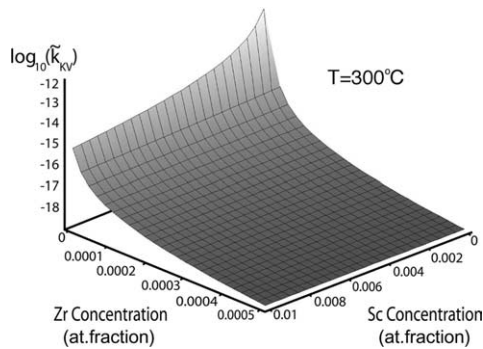


Fig. 13. Calculated normalized coarsening rate constant at 300 °C vs. Zr and Sc concentrations obtained utilizing Eq. (4).

that the KV model does not account for a precipitate volume fraction effect.

## 5. Conclusions

In a series of coarsening experiments, the temporal behavior of Al(Sc,Zr) alloys was studied by TEM and HREM, and compared to the results for Al(Sc) alloys [26]. These experiments and their analyses result in the following findings:

- Part I [1] demonstrated that the precipitate chemical composition is temporally changing during the process of coarsening, which is discussed in detail in Part II.
- The exact morphology of  $\text{Al}_3(\text{Sc}_{1-x}\text{Zr}_x)$  precipitates was examined for the first time, employing HREM, in Al(Sc,Zr) alloys aged at 300 °C (Fig. 1).  $\text{Al}_3(\text{Sc}_{1-x}\text{Zr}_x)$  precipitates in all ternary alloys are observed to have facets parallel to the  $\{100\}$  and  $\{110\}$  planes and, therefore, they are close to being great rhombicuboctahedra.
- The effect of  $\text{Al}_3(\text{Sc}_{1-x}\text{Zr}_x)$  precipitate volume fraction and Zr additions on precipitate morphology was observed. Alloys with  $<0.004$  volume fractions of  $\text{Al}_3(\text{Sc}_{1-x}\text{Zr}_x)$  precipitates contain precipitates that are initially spheroids, which evolve to cuboids, and finally lobed cuboids; in contrast, alloys with  $\geq 0.007$  volume fractions of  $\text{Al}_3(\text{Sc}_{1-x}\text{Zr}_x)$  precipitates do not exhibit lobed cuboids.  $\text{Al}_3\text{Sc}$  precipitates in Al-0.07 at.% Sc alloys are known to be irregularly shaped [26], while additions of Zr produce faceted  $\text{Al}_3(\text{Sc}_{1-x}\text{Zr}_x)$  precipitates at a higher number density than the Al-0.07 at.% Sc alloy.

- $\text{Al}_3(\text{Sc}_{1-x}\text{Zr}_x)$  precipitates temporally evolve morphologically from spheroids to cuboids to lobed cuboids (Figs. 2 and 3).
- The effect of elastic anisotropy on the formation of lobed cuboids in Al-0.06 Sc-0.005 Zr and Al-0.07 Sc-0.019 Zr alloys aged at 350 and 375 °C is discussed, where small volume fractions ( $<0.004$ ) of precipitates permit coarsening to occur with smaller elastic and diffusional interactions than the higher volume fraction ( $>0.007$ ) alloys.
- Time exponents for coarsening are determined from the slopes of double logarithmic plots of average precipitate radius,  $\langle R \rangle$ , vs. aging time (Eq. (1), Fig. 5) and precipitate number density,  $N_V$ , vs. aging time (Eq. (2), Fig. 6). Part I [1] presents a determination utilizing the matrix supersaturation vs. aging time (Eq. (3)). The calculated time exponents for coarsening range from 0.02 to 0.21 ( $\langle R \rangle$  vs.  $t$ , Table 2) and 0.00072 to  $-0.39$  ( $N_V$  vs.  $t$ , Table 3), which are significantly less than the values of  $1/3$  and  $-1$ , respectively, predicted by UOKV model for diffusion-limited coarsening of a ternary alloy. From the matrix supersaturation vs. aging time [1] time exponents for coarsening for Sc =  $-0.33$  and Zr =  $-0.15$  are calculated, compared to the predicted value of  $-1/3$ .
- Agreement with the UOKV model of a ternary alloy is not achieved for the following reasons: (a) accurate time exponents for coarsening are difficult to calculate when precipitates do not coarsen significantly, as is the case for Al(Sc,Zr) alloys and therefore the time exponents are effective values; and (b) the precipitate size distributions (PSDs) are not self-similar.
- Assuming diffusion-limited coarsening, experimental coarsening rates,  $k_{\text{exp}}$ , are determined for Al(Sc,Zr) alloys aged at 300, 350, or 375 °C (Table 4), and compared to the model coarsening rates,  $k_{\text{KV}}$ , obtained from Eq. (1) [7]. Adding Zr was found to decrease the coarsening rate of  $\text{Al}_3(\text{Sc}_{1-x}\text{Zr}_x)$  precipitates compared to Al(Sc) alloys with the same volume fraction of  $\text{Al}_3\text{Sc}$  precipitates [26] (Fig. 11).
- A change in the  $\text{Al}_3(\text{Sc}_{1-x}\text{Zr}_x)$  precipitate coherency is observed to have a dramatic effect on the coarsening rate, as observed by the discontinuity in slope for two Al(Sc,Zr) alloys aged at 375 °C, Fig. 11. Once  $\text{Al}_3(\text{Sc}_{1-x}\text{Zr}_x)$  precipitates lose full coherency, the coarsening rate constant increases due to an increase in the interfacial free energy of the precipitates.

- Temperature-corrected effective activation energies for diffusion-limited coarsening are experimentally determined (Table 5) and compared to the literature values for diffusion of Sc and Zr in Al (Table 6). Al-0.07 Sc-0.019 Zr, Al-0.06 Sc-0.005 Zr, and Al-0.09 Sc-0.047 Zr alloys have temperature-corrected experimental activation energies of  $258 \pm 37$ ,  $240 \pm 15$ , and  $281 \pm 17$  kJ mol<sup>-1</sup>, respectively, and are, within experimental error for the Al-0.06 Sc-0.005 Zr and Al-0.07 Sc-0.019 Zr alloys, close to the literature activation energy values for diffusion of Zr in Al (222 [65] and 242 kJ mol<sup>-1</sup> [3]).
- In contrast, the Al-0.14 Sc-0.012 Zr alloy is found to have an experimental activation energy of  $134 \pm 28$  kJ mol<sup>-1</sup>, which is, within experimental error, near the literature values for the activation energy for diffusion of Sc in Al (174 [66], 154 [67], and  $164 \pm 9$  kJ mol<sup>-1</sup> [26]).
- The previous two points imply that coarsening of the Al-0.07 Sc-0.019 Zr, Al-0.06 Sc-0.005 Zr, and Al-0.09 Sc-0.047 Zr alloys is controlled by volume diffusion of Zr in Al, and coarsening of the Al-0.14 Sc-0.012 Zr alloy is controlled by volume diffusion of Sc in Al.
- From the above conclusions, coarsening models for ternary alloys are not obeyed in detail because Zr diffuses significantly slower in Al than does Sc, so obtaining global equilibrium (between 300 and 375 °C) is not possible within reasonable time periods. The neglect of the off-diagonal terms in the diffusion tensor is an assumption of the KV model of coarsening of ternary alloys, which implies that a significant amount of flux is not carried by the off-diagonal terms and this may be incorrect.

## Acknowledgements

This research was supported by the United States Department of Energy, Basic Energy Sciences Division, under Contract DE-FG02-98ER45721. We thank David C. Dunand, Peter W. Voorhees, Emmanuelle A. Marquis, Jens Alkemper, and Alexander Umantsev for scientific discussions. Special thanks to Argonne National Laboratories and Dr. Roseann Csencsits for use of the JEOL 4000EXII. We thank Ashurst Inc. for supplying a Al–Sc master alloy and Robert Hyland, Jr. at Alcoa, Inc. for supplying Al–Sc and Al–Zr master alloys and helpful discussions.

## References

- [1] Fuller CB, Seidman DN. Acta Mater 2005;53:5401.
- [2] Fujikawa S-I, Sugaya M, Takei H, Hirano K-I. J Less-Common Met 1979;63:87.
- [3] Hirano K, Fujikawa S. J Nucl Mater 1978;69–70:564.
- [4] Lifshitz IM, Slyozov VV. J Phys Chem Solids 1961;19:35.
- [5] Wagner C. Z Elektrochem 1961;65:581.
- [6] Umantsev A, Olson G. Scr Metall 1993;29:1135.
- [7] Kuehmann CJ, Voorhees PW. Metall Mater Trans A 1996;27A:937.
- [8] Calderon HA, Voorhees PW, Murray JL, Kostorz G. Acta Metall Mater 1994;42:991.
- [9] Ardell AJ. Interf Sci 1995;3:119.
- [10] Cho JH, Ardell AJ. Acta Mater 1998;46:5907.
- [11] Elagin VI, Zakharov VV, Rostova TD. Metal Sci Heat Treat Metals 1992;1:37.
- [12] Toropova LS, Kamardinkin AN, Kindzhibalo VV, Tyvanchuk AT. Phys Met Metallogr 1990;70:106.
- [13] Harada Y, Dunand DC. Mater Sci Eng A 2002;329–331:686.
- [14] Davydov VG, Elagin VI, Zakharov VV, Rostova TD. Metal Sci Heat Treat 1996;38:347.
- [15] Elagin VI, Zakharov VV, Pavlenko SG, Rostova TD. Phys Met Metallogr 1985;60:88.
- [16] Robson JD. Acta Mater 2004;52:1409.
- [17] Drits ME, Toropova LS, Bykov YG. Metals science, casting, processing of light alloys. Moscow: Metallurgiya; 1986.
- [18] Martin JW, Humphreys FJ. Scr Metall 1974;8:679.
- [19] Footner PK, Richards BP. J Mater Sci 1982;17:2141.
- [20] Ricks RA, Porter AJ, Ecob RC. Acta Metall 1983;31:43.
- [21] Njan N, Dimitrov O. Acta Metall 1989;37:2559.
- [22] MacKay RA, Nathal MV. Acta Metall Mater 1990;38:933.
- [23] Fahrman M, Fratzl P, Paris O, Fahrman E, Johnson WC. Acta Metall Mater 1995;43:1007.
- [24] Fahrman M, Fahrman E, Pollock TM, Johnson WC. Metall Mater Trans A 1997;28A:1943.
- [25] Ardell AJ, Kim DM. Phase transformations and evolution in materials. In: Turchi PEA, Gonis A, editors. Warrendale (PA): TMS; 2000. p. 309.
- [26] Marquis EA, Seidman DN. Acta Mater 2001;49:1909.
- [27] Hyland RW. Metall Trans A 1992;23A:1947.
- [28] Novotny GM, Ardell AJ. Mater Sci Eng A 2001;A318:144.
- [29] Fuller CB. Ph.D. thesis. Northwestern University: Evanston, IL; 2003.
- [30] Marquis EA. Ph.D. thesis. Northwestern University: Evanston, IL; 2002.
- [31] Fuller CB, Seidman DN, Dunand DC. Scr Metall 1999;40:691.
- [32] Harada Y, Dunand DC. Acta Metall 2000;48:3477.
- [33] Harada Y, Dunand DC. In: Proceedings of the 7th international conference on creep and fatigue at elevated temperature (Creep VII). Japan Society of Mechanical Engineers: Tokyo, Japan; 2001. p. 219.
- [34] Fuller CB, Krause AR, Dunand DC, Seidman DN. Mater Sci Eng A 2002;A338:8.
- [35] Marquis EA, Seidman DN, Dunand DC. Creep of precipitation strengthened Al(Sc) alloys. In: Mishra RS, Earthman JC, Raj SV, editors. Creep deformation: fundamentals and applications. Warrendale (PA): TMS; 2002. p. 299.
- [36] Marquis EA, Seidman DN. Microsc Microanal 2002;8:1100CD.
- [37] Marquis EA, Dunand DC. Scr Mater 2002;47:503.
- [38] Harada Y, Dunand DC. Scr Mater 2003;48:219.
- [39] Marquis EA, Seidman DN, Dunand DC. Acta Mater 2003;50:4021.
- [40] Marquis EA, Seidman DN, Dunand DC. Microstructural and creep properties of an Al-2 Mg-0.2 Sc (wt.%) alloy. In: Jin ABZ, Bieler TA, Radhakrishnan B, editors. Hot deformation of aluminum alloys III. Warrendale (PA): TMS; 2003. p. 177.
- [41] Fuller CB, Seidman DN, Dunand DC. Structure–property relationships of Al(Sc,Zr) alloys at 24 and 300 °C. In: Jin ABZ, Bieler TA, Radhakrishnan B, editors. Hot deformation of aluminum alloys III. Warrendale (PA): TMS; 2003. p. 531.
- [42] Fuller CB, Seidman DN, Dunand DC. Acta Mater 2003;51:4803.
- [43] Marquis EA, Seidman DN, Dunand DC. Acta Mater 2003;51:4751.
- [44] Marquis EA, Seidman DN, Asta M, Woodward CM, Ozolin V. Phys Rev Lett 2003;91:036101-1.
- [45] Marquis EA, Seidman DN. Acta Mater 2005;53:4259.
- [46] Kelly PM. Metals Forum 1982;5:13.
- [47] Brailsford AD, Wynblatt P. Acta Metall 1979;27:489.
- [48] Voorhees PW. Annu Rev Mater Sci 1992;22:197.
- [49] Wagner R, Kampmann R, Voorhees P. Homogeneous second-phase precipitation. In: Kostorz G, editor. Phase transformations in materials. New York (NY): Wiley-VCH; 2001. p. 309.

- [50] Lee JK. *Theor Appl Fract Mech* 2000;33:207.
- [51] Marqusee JA, Ross J. *J Chem Phys* 1983;79:373.
- [52] Voorhees PW. *J Stat Phys* 1985;38:231.
- [53] Marsh SP, Glicksman ME. *Acta Metall* 1996;44:3761.
- [54] Ratke L, Voorhees PW. *Growth and coarsening: ripening in materials processing*. Berlin: Springer; 2002.
- [55] Binder K, Stauffer D. *Phys Rev Lett* 1974;33:1006.
- [56] Binder K. *Phys Rev B* 1977;15:4425.
- [57] Roussel J-M, Bellon P. *Phys Rev B* 2001;63:184114.
- [58] Shewmon PG. *Trans TMS-AIME* 1965;233:736.
- [59] Maheshwari A, Ardell AJ. *Acta Metall Mater* 1992;40:2661.
- [60] Kim DM, Ardell AJ. *Scr Mater* 2000;43:381.
- [61] Voorhees PW, personal communications; 2002.
- [62] Asta M, Foiles SM, Quong AA. *Phys Rev B* 1998;57:11265.
- [63] Schmuck C, Caron P, Hauet A, Blavette D. *Philos Mag* 1997;76:527.
- [64] Chen YC, Fine ME, Weertman JR. *Acta Metall Mater* 1990;38:771.
- [65] Zedalis MS, Fine ME. *Metall Trans A* 1986;17A:2187.
- [66] Fujikawa S-I. *Defect Diff Forum* 1997;143–147:115.
- [67] Ozolins V, Asta M, unpublished results.